Journal of Computational Physics **150,** 518–548 (1999)
Article ID jcph.1999.6203, available online at http://www.idealibrary.com on IDEAL®

Quasi-3D Navier–Stokes Model for a Rotating Airfoil

Wen Zhong Shen and Jens Nørkær Sørensen

Department of Energy Engineering, Technical University of Denmark, 2800 Lyngby, Denmark
E-mail: shen@et.dtu.dk, jns@et.dtu.dk

Received March 25, 1998; revised January 11, 1999

A quasi-3D model of the unsteady Navier–Stokes equations in a rotating frame of reference has been developed. The equations governing the flow past a rotating blade are approximated using an order of magnitude analysis on the spanwise derivatives. The model takes into account rotational effects and spanwise outflow at computing expenses in the order of what is typical for similar 2D calculations. Results are presented for both laminar and turbulent flows past blades in pure rotation. In the turbulent case the influence of small-scale turbulence is modelled by the one-equation Baldwin–Barth turbulence model. The computations demonstrate that the main influence of rotation is to increase the maximum lift.

1. INTRODUCTION

The design of blade shapes for wind turbines is typically based on employing the blade-element momentum-theory (BEM) with lift and drag forces determined from 2D measurements. The results obtained are reasonable in the vicinity of the design point, but in stalled conditions the BEM is known to underpredict the forces acting on the blades (see, e.g., Rasmussen [11]).

A likely explanation for the underprediction is that the flow is not adequately modelled by static 2D airfoil data in the stalled regime. From experiments it is evident that radial flow exists in the bottom of separated boundary layers on rotating wings and it is likely that this alters the lift and drag characteristics of the individual airfoil section. The physics behind this is that the outflow induces a Coriolis force in the chordwise direction which acts as a favorable pressure gradient that tends to delay boundary layer separation.

These 3D effects were first described by Himmelskamp [7], who found lift coefficients as high as 3 near the hub of a fan blade. Later experiments are due to Milborrow and Ross [9] who carried out a wind tunnel study of the loading on a model rotor. Here, it was found that

0021-9991/99 $30.00

the effective lift coefficient was higher than that obtained from 2D data. Using balanced wind vanes Savino and Nyland [13] made it possible to visualize the flow direction on the surface of a full-scale rotor. They found a chordwise flow upstream of the separation line, whereas the flow in the separated regions was strongly radial. Later experiments carried out by, e.g., Ronsten [12] and Bruining *et al.* [3] support these observations.

In an analysis by Fogarty [5] it was shown that 3D cross flow effects are small for attached boundary layers on a rotating blade. As a conclusion, Fogarty suggested that the observed deviations from 2D behaviour only occur for separated boundary layers. From flow visualizations on a rotating blade, the same was noted by McCroskey [8] who observed separated flow to be dominated by a significant radial flow component, whereas the location of the separation line did not change appreciably. In Appendix A we show that the spanwise velocity component compared to the chordwise component scales as $(c/z)^p$, where c is the chord length and z is the spanwise distance measured from the rotational axis, with $p = 1$ for attached flow and $p = -1/3$ for separated flow. Thus, near the rotational axis where $c/z = O(1)$ rotational effects are expected to have a significant impact on the airfoil characteristics for both attached and separated flows. On the outer part of the blade, however, rotational effects are mainly related to separated flow.

To provide more representative airfoil data for use in rotor-performance calculations, it is necessary to derive synthesized 3D data either from experiments or from calculations. For many reasons it is difficult, however, to extract the data solely from experiments. First, data from model experiments are of minor value as the Reynolds number, which is a crucial model parameter, has to be very close to reality. Second, in a full-scale experiment it is a difficult, if not impossible, task to derive local airfoil data which is not polluted by secondary effects, such as turbulent inflow, tower blockage, etc. This is furthermore complicated by the problem of determining the local angle of attack correctly. On the other hand, solving the full 3D Navier–Stokes equations in a rotating frame of reference is known to be very computing consuming and it is not evident how the results from global 3D Navier–Stokes solutions may be employed to determine local airfoil characteristics.

Thus there is a need for a method which is computationally reasonable at the same time as it is capable of predicting leading 3D effects on a rotating blade in attached as well as in stalled conditions.

In the proposed model, presented in the following, the full Navier–Stokes equations are approximated using an order of magnitude analysis on the spanwise derivatives. This results in a quasi-3D formulation in which rotational effects and radial flow components are maintained. As a result, the calculation needs only to be carried out on a 2D airfoil, hence reducing the computing costs in the order of what is typical for a pure 2D calculation. Earlier, similar approaches have been made in fixed-wing aerodynamics by applying the infinite-swept-wing approximation on the boundary layer equations, see, e.g., [4, 10]. For a rotating blade, such an approximation has been implemented and used in viscous/inviscid coupling algorithms [17, 18]. However, this is the first time it has been applied on the unsteady Navier–Stokes equations in a rotating frame of reference.

The paper is organized as follows. In Section 2, the hypothesis employed in the spanwise direction of the rotating airfoil is discussed and followed by a set of quasi-3D Navier–Stokes equations. In Section 3, a Baldwin–Barth turbulence model for the quasi-3D model is given. The numerical implementation is presented in Section 4. Numerical results for laminar as well as turbulent flows are presented in Section 5.

2. FORMULATION OF THE PROBLEM

Consider a blade section performing a rotating motion. Let $(oxyz)$ be the rotating reference system associated with constant angular velocity Ω_y and let oz define the spanwise direction of the blade. Define by $\mathbf{u} = (u, v, w)$ the velocity and by $\boldsymbol{\omega} = (\omega_x, \omega_y, \omega_z)$ the vorticity in the rotating reference system.

2.1. *Hypotheses*

By considering the flow around an infinite cylinder of arbitrary cross-section rotating steadily about the (negative) y-axis (see Fig. 1) it was shown by Sears [14] that the inviscid velocity components may be written as

$$u = \Omega_y z \frac{\partial \phi}{\partial x}, \tag{1}$$

$$v = \Omega_y z \frac{\partial \phi}{\partial y}, \tag{2}$$

$$w = \Omega_y [2x - \phi], \tag{3}$$

where $\phi = \phi(x, y)$ denotes the equivalent 2D velocity potential due to a blade in translational movement with unit speed in the negative x-direction. It is readily seen that the velocity components u and v are given in a form as would be expected from a simple 2D analysis. It is not obvious, however, that the spanwise velocity component can be expressed in a simple formula which depends only on the velocity potential of the equivalent 2D flow.

In the later analysis of Fogarty and Sears [6] it was shown that the expression for the spanwise velocity component is the same even if the blade is advancing in the direction perpendicular to the plane of rotation, i.e., the y-direction. To derive an extended 2D approach in which the important effects of Coriolis and centrifugal forces are included we now seek a plausible approximation that allows us to get rid of the spanwise derivatives in the 3D equations. An approximation that is consistent with Eqs. (1)–(3) is to assume the following similarity expressions for the velocity components

$$u = f(x, y)z, \tag{4}$$

$$v = g(x, y)z, \tag{5}$$

$$w = h(x, y). \tag{6}$$

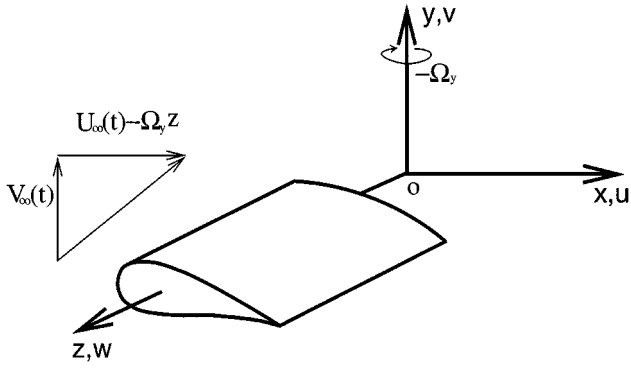

FIG. 1. Definition of the coordinates.

These expressions then lead to the basic hypothesis

$$\frac{\partial u}{\partial z} = \frac{u}{z}, \tag{7}$$

$$\frac{\partial v}{\partial z} = \frac{v}{z}, \tag{8}$$

$$\frac{\partial w}{\partial z} = 0. \tag{9}$$

In the boundary layer, Eqs. (4)–(6) assume similarity with a scaling of the spanwise distance, z, for the chordwise velocity components. The spanwise velocity distribution is assumed to be the same at all spanwise positions. This obviously introduce deviations, as compared to a full 3D representation, that are difficult to quantify completely. However, in Appendix A we have made an order of magnitude analysis of the terms that are modified or neglected in the full 3D equations. From this it is found that in the worst case the error will be of $O(c/z)^2$ for attached flow and of $O(c/z)^{2/3}$ in the case of separation. It should be noted, however, that the aim of the quasi-3D model is to enrich a 2D airfoil code with effects from the influence of Coriolis and centrifugal forces. Thus, employing Eqs. (7)–(9) to neglect terms containing z-derivatives a set of equations may be derived that is much simpler than the full 3D equations and which contains 3D terms to leading order in c/z for both attached and separated flows.

2.2. *Formulation in Cartesian Coordinates*

The motion of a viscous incompressible flow in a rotating reference system is governed by the time-averaged Navier–Stokes equations

$$\frac{\partial \mathbf{u}}{\partial t} + \nabla \times \mathbf{u} \times \mathbf{u} + 2\boldsymbol{\Omega} \times \mathbf{u} + \frac{\partial \boldsymbol{\Omega}}{\partial t} \times \mathbf{r} = -\nabla P + \frac{\partial}{\partial x_j}\left[(\nu + \nu_t)\left(\frac{\partial \mathbf{u}}{\partial x_j} + \nabla u_j\right)\right], \tag{10}$$

$$\nabla \cdot \mathbf{u} = 0, \tag{11}$$

where $\boldsymbol{\Omega} = (0, \Omega_y, 0)$ and the total pressure $P = p/\rho + |\mathbf{u}|^2/2 + (\boldsymbol{\Omega} \cdot \mathbf{r})^2/2 - \Omega^2 r^2/2$, with p denoting the static pressure, ρ the density, ν the kinematic viscosity, and $\mathbf{r}$ the position vector. The Reynolds stresses are modelled by introducing an eddy viscosity ν_t,

$$-\overline{u_i' u_j'} = \nu_t\left(\frac{\partial u_i}{\partial x_j} + \frac{\partial u_j}{\partial x_i}\right), \tag{12}$$

where u_i' denotes a fluctuating velocity component and $\overline{(\,)}$ is the time-averaging.

In Eq. (10), the diffusion term contains a derivative of ν_t with respect to z. This requires an additional hypothesis for ν_t. For simplicity, we assume that

$$\frac{\partial \nu_t}{\partial z} = 0. \tag{13}$$

Using the hypothesis (7), we get

$$\frac{\partial^2 u}{\partial z^2} = \frac{\partial}{\partial z}\left(\frac{\partial u}{\partial z}\right) = \frac{\partial}{\partial z}\left(\frac{u}{z}\right) = \frac{z\partial u/\partial z - u}{z^2} = \frac{z(u/z) - u}{z^2} = 0.$$

Using the hypotheses (8) and (9), similar expressions are obtained for the other velocity components

$$\frac{\partial^2 v}{\partial z^2} = 0,$$
$$\frac{\partial^2 w}{\partial z^2} = 0.$$

As a result the z-derivatives of the diffusion terms vanish

$$\frac{\partial}{\partial z}\left[(\nu+\nu_t)\left(\frac{\partial \mathbf{u}}{\partial z}+\nabla w\right)\right] = \frac{\partial(\nu+\nu_t)}{\partial z}\left(\frac{\partial \mathbf{u}}{\partial z}+\nabla w\right)+(\nu+\nu_t)\left[\frac{\partial^2 u}{\partial z^2}+\nabla\left(\frac{\partial w}{\partial z}\right)\right] = 0.$$

We now consider the vorticity definition. Using the hypothesis discussed in Subsection 2.1, the quasi-3D vorticity definition is given as

$$\omega_x = \frac{\partial w}{\partial y} - \frac{v}{z}, \tag{14}$$
$$\omega_y = \frac{u}{z} - \frac{\partial w}{\partial x}, \tag{15}$$
$$\omega_z = \frac{\partial v}{\partial x} - \frac{\partial u}{\partial y}. \tag{16}$$

In Eq. (10), the only z-derivative left is the pressure. But there is no hypothesis, neither for the static pressure p nor for the total pressure P. To overcome this difficulty, we consider the curl operator defined above, $(\partial/\partial x, \partial/\partial y, 1/z)\times$, and keep in mind that the curl of a gradient operator is zero. Then the only possible hypothesis for the pressure is that

$$\frac{\partial(p+|\mathbf{u}|^2/2+(\mathbf{\Omega}\cdot\mathbf{r})^2/2-\Omega^2 r^2/2)}{\partial z} = \frac{(p+|\mathbf{u}|^2/2+(\mathbf{\Omega}\cdot\mathbf{r})^2/2-\Omega^2 r^2/2)}{z}. \tag{17}$$

From Eqs. (9) and (11), the divergence of the velocity becomes

$$\frac{\partial u}{\partial x}+\frac{\partial v}{\partial y} = 0.$$

Then the quasi-3D formulation in velocity-pressure variables reads

$$\frac{\partial u}{\partial t}+w\omega_y - v\omega_z + 2w\Omega_y = -\frac{\partial P}{\partial x}+2\frac{\partial}{\partial x}\left(\nu^*\frac{\partial u}{\partial x}\right)+\frac{\partial}{\partial y}\left[\nu^*\left(\frac{\partial u}{\partial y}+\frac{\partial v}{\partial x}\right)\right], \tag{18}$$
$$\frac{\partial v}{\partial t}+u\omega_z - w\omega_x = -\frac{\partial P}{\partial y}+\frac{\partial}{\partial x}\left[\nu^*\left(\frac{\partial u}{\partial y}+\frac{\partial v}{\partial x}\right)\right]+2\frac{\partial}{\partial y}\left(\nu^*\frac{\partial v}{\partial y}\right), \tag{19}$$
$$\frac{\partial w}{\partial t}+v\omega_x - u\omega_y - 2u\Omega_y = -\frac{P}{z}+\frac{\partial}{\partial x}\left(\nu^*\frac{\partial w}{\partial x}\right)+\frac{\partial}{\partial y}\left(\nu^*\frac{\partial w}{\partial y}\right), \tag{20}$$
$$\frac{\partial u}{\partial x}+\frac{\partial v}{\partial y} = 0, \tag{21}$$

where $\nu^* = \nu + \nu_t$.

In the present work we prefer to employ the velocity-vorticity form of the Navier–Stokes equations because the algorithm forming the basis for the model is formulated in velocity-vorticity variables (see [15]).

Taking the curl of Eqs. (18)–(20) we get

$$\frac{\partial \omega_x}{\partial t} + \frac{\partial}{\partial y}(v\omega_x - u(\omega_y + 2\Omega_y)) + \frac{w\omega_x}{z} - \frac{u\omega_z}{z} = \frac{\partial^2(\nu^*\omega_x)}{\partial y^2} - \frac{\partial^2(\nu^*\omega_y)}{\partial x \partial y} - \frac{1}{z}\frac{\partial(\nu^*\omega_z)}{\partial x} + \frac{2}{z}\left(\frac{\partial^2 \nu^*}{\partial x \partial y}u + \frac{\partial^2 \nu^*}{\partial y^2}v\right), \tag{22}$$

$$\frac{\partial \omega_y}{\partial t} + \frac{\partial}{\partial x}(u(\omega_y + 2\Omega_y) - v\omega_x) - \frac{v\omega_z}{z} + \frac{w(\omega_y + 2\Omega_y)}{z} = \frac{\partial^2(\nu^*\omega_y)}{\partial x^2} - \frac{\partial^2(\nu^*\omega_x)}{\partial x \partial y} - \frac{1}{z}\frac{\partial(\nu^*\omega_z)}{\partial y} - \frac{2}{z}\left(\frac{\partial^2 \nu^*}{\partial x^2}u + \frac{\partial^2 \nu^*}{\partial x \partial y}v\right), \tag{23}$$

$$\frac{\partial \omega_z}{\partial t} + \frac{\partial(u\omega_z)}{\partial x} + \frac{\partial(v\omega_z)}{\partial y} - \frac{\partial(w\omega_x)}{\partial x} - \frac{\partial(w(\omega_y + 2\Omega_y))}{\partial y} = \left(\frac{\partial^2}{\partial x^2} + \frac{\partial^2}{\partial y^2}\right)[\nu^*\omega_z] + 2\left(\frac{\partial^2 \nu^*}{\partial x^2}\frac{\partial u}{\partial y} + \frac{\partial^2 \nu^*}{\partial x \partial y}\frac{\partial v}{\partial y} - \frac{\partial^2 \nu^*}{\partial x \partial y}\frac{\partial u}{\partial x} - \frac{\partial^2 \nu^*}{\partial y^2}\frac{\partial v}{\partial x}\right). \tag{24}$$

The divergence of the velocity, Eq. (21), implies the existence of a stream function, ψ, in the z-direction such that

$$u = -\frac{\partial \psi}{\partial y}, \tag{25}$$

$$v = \frac{\partial \psi}{\partial x}. \tag{26}$$

From the vorticity definition, Eq. (16), a Poisson equation for ψ is obtained

$$\frac{\partial^2 \psi}{\partial x^2} + \frac{\partial^2 \psi}{\partial y^2} = \omega_z. \tag{27}$$

In order to ensure equivalence between the present formulation and that of the primitive variables, the uniformity of the pressure, which determines the value of the stream function at the airfoil surface, is added

$$\oint_c \left[\frac{\partial((\mathbf{u} + \boldsymbol{\Omega} \times \mathbf{r}) \cdot \mathbf{s})}{\partial t} + \mathbf{u} \cdot \mathbf{n}\omega_z - w(\boldsymbol{\omega} + 2\boldsymbol{\Omega}) \cdot \mathbf{n} - \nu\frac{\partial \omega_z}{\partial n}\right] ds = 0, \tag{28}$$

where c is any closed path around the airfoil, $\mathbf{s}$ is the tangent vector, and $\mathbf{n}$ the normal vector to the surface.

The equation of the velocity component in the z-direction is obtained by combining the vorticity definition, Eqs. (14) and (15), with Eq. (21)

$$\frac{\partial^2 w}{\partial x^2} + \frac{\partial^2 w}{\partial y^2} = \frac{\partial \omega_x}{\partial y} - \frac{\partial \omega_y}{\partial x}. \tag{29}$$

2.3. *Formulation in Curvilinear Coordinates*

The computational grid is generated using a conformal mapping (see Appendix B). The mesh is orthogonal and stretched in the radial direction of the airfoil. Denoting by (ξ, η) the coordinates in the transformed plane, the transformation Jacobian is given by

$$J = \xi_x \eta_y - \xi_y \eta_x,$$

and the Jacobian of the inverse transformation is

$$J^{-1} = x_\xi y_\eta - x_\eta y_\xi.$$

Since the grid is orthogonal, we have $x_\eta x_\xi + y_\xi y_\eta = 0$. Define the contra-variant velocity components

$$u^c = y_\eta u - x_\eta v, \tag{30}$$

$$v^c = -y_\xi u + x_\xi v, \tag{31}$$

and the contra-variant vorticity components

$$\omega_x^c = y_\eta \omega_x - x_\eta \omega_y, \tag{32}$$

$$\omega_y^c = -y_\xi \omega_x + x_\xi \omega_y. \tag{33}$$

Introducing $\alpha = y_\eta / x_\xi$, in curvilinear coordinates the vorticity definitions become

$$\omega_x^c = \frac{\partial w}{\partial \eta} - \frac{\alpha v^c}{z}, \tag{34}$$

$$\omega_y^c = \frac{u^c}{\alpha z} - \frac{\partial w}{\partial \xi}, \tag{35}$$

$$J^{-1}\omega_z = \frac{\partial (\alpha v^c)}{\partial \xi} - \frac{\partial}{\partial \eta}\left(\frac{u^c}{\alpha}\right), \tag{36}$$

and the divergence of the vorticity takes the form

$$J^{-1} \nabla \cdot \boldsymbol{\omega} = \frac{\partial \omega_x^c}{\partial \xi} + \frac{\partial \omega_y^c}{\partial \eta} + \frac{J^{-1}\omega_z}{z} = 0. \tag{37}$$

The contra-variant velocity components are transformed from the definition of the stream function ψ

$$u^c = -\frac{\partial \psi}{\partial \eta}, \tag{38}$$

$$v^c = \frac{\partial \psi}{\partial \xi}. \tag{39}$$

For convenience, the absolute vorticity is employed as a variable

$$\omega_x^{c*} = y_\eta \omega_x - x_\eta(\omega_y + 2\Omega_y), \tag{40}$$

$$\omega_y^{c*} = -y_\xi \omega_x + x_\xi(\omega_y + 2\Omega_y), \tag{41}$$

$$\omega_z^{*} = \omega_z. \tag{42}$$

Additional terms from the turbulence modelling are defined as

$$F_1 = 2\frac{\partial u}{\partial x}\frac{\partial \nu_t}{\partial x} + 2\frac{\partial v}{\partial x}\frac{\partial \nu_t}{\partial y}, \tag{43}$$

$$F_2 = 2\frac{\partial u}{\partial y}\frac{\partial \nu_t}{\partial x} + 2\frac{\partial v}{\partial y}\frac{\partial \nu_t}{\partial y}, \tag{44}$$

$$\begin{aligned} F_3 &= 2\frac{u}{z}\frac{\partial \nu_t}{\partial x} + 2\frac{v}{z}\frac{\partial \nu_t}{\partial y} \\ &= \frac{2}{zJ^{-1}}\left(u^c\frac{\partial \nu_t}{\partial \xi} + v^c\frac{\partial \nu_t}{\partial \eta}\right). \end{aligned} \tag{45}$$

In the (ξ, η) coordinate system, the final vorticity transport equations take the form

$$\begin{aligned} &\frac{\partial \omega_x^{c*}}{\partial t} + \frac{\partial}{\partial \eta}\left(\frac{v^c\omega_x^{c*} - u^c\omega_y^{c*}}{J^{-1}}\right) - \frac{\left(u^c\omega_z^{*} - w\omega_x^{c*}\right)}{z} \\ &\quad = -\frac{\partial}{\partial \eta}\left[\frac{1}{J^{-1}}\frac{\partial}{\partial \xi}\left(\alpha\nu^*\omega_y^{c*}\right) - \frac{1}{J^{-1}}\frac{\partial}{\partial \eta}\left(\frac{\nu^*\omega_x^{c*}}{\alpha}\right)\right] - \frac{\alpha}{z}\frac{\partial(\nu^*\omega_z^{*})}{\partial \xi} + \frac{\partial F_3}{\partial \eta} - \frac{\alpha F_2^c}{z}, \end{aligned} \tag{46}$$

$$\begin{aligned} &\frac{\partial \omega_y^{c*}}{\partial t} + \frac{\left(w\omega_y^{c*} - v^c\omega_z^{*}\right)}{z} - \frac{\partial}{\partial \xi}\left(\frac{v^c\omega_x^{c*} - u^c\omega_y^{c*}}{J^{-1}}\right) \\ &\quad = -\frac{1}{\alpha z}\frac{\partial(\nu^*\omega_z^{*})}{\partial \eta} + \frac{\partial}{\partial \xi}\left[\frac{1}{J^{-1}}\frac{\partial}{\partial \xi}\left(\alpha\nu^*\omega_y^{c*}\right) - \frac{1}{J^{-1}}\frac{\partial}{\partial \eta}\left(\frac{\nu^*\omega_x^{c*}}{\alpha}\right)\right] + \frac{F_1^c}{\alpha z} - \frac{\partial F_3}{\partial \xi}, \end{aligned} \tag{47}$$

$$\begin{aligned} &\frac{\partial(J^{-1}\omega_z^{*})}{\partial t} + \frac{\partial}{\partial \xi}\left(u^c\omega_z^{*} - w\omega_x^{c*}\right) + \frac{\partial}{\partial \eta}\left(v^c\omega_z^{*} - w\omega_y^{c*}\right) \\ &\quad = \frac{\partial}{\partial \xi}\left[\alpha\frac{\partial(\nu^*\omega_z^{*})}{\partial \xi}\right] + \frac{\partial}{\partial \eta}\left[\frac{1}{\alpha}\frac{\partial(\nu^*\omega_z^{*})}{\partial \eta}\right] + \frac{\alpha F_2^c}{\partial \xi} - \frac{\partial}{\partial \eta}\left(\frac{F_1^c}{\alpha}\right), \end{aligned} \tag{48}$$

where (F_1^c, F_2^c) is the contra-variant form of (F_1, F_2).

The Poisson equations for the stream function and velocity component in the z-direction become

$$\frac{\partial}{\partial \xi}\left(\alpha\frac{\partial \psi}{\partial \xi}\right) + \frac{\partial}{\partial \eta}\left(\frac{1}{\alpha}\frac{\partial \psi}{\partial \eta}\right) = J^{-1}\omega_z, \tag{49}$$

$$\frac{\partial}{\partial \xi}\left(\alpha\frac{\partial w}{\partial \xi}\right) + \frac{\partial}{\partial \eta}\left(\frac{1}{\alpha}\frac{\partial w}{\partial \eta}\right) = \frac{\partial}{\partial \eta}\left(\frac{\omega_x^c}{\alpha}\right) - \frac{\partial\left(\alpha\omega_y^c\right)}{\partial \xi}. \tag{50}$$

The uniformity condition of the pressure takes the form

$$\oint_c \left[\frac{\partial(\alpha v^c)}{\partial t} + u^c\omega_z^{*} - w\omega_x^{c*} - \alpha\frac{\partial(\nu^*\omega_z^{*})}{\partial \xi} + \alpha\dot{\Omega}_z(xx_\xi + yy_\xi)\right]d\eta = 0. \tag{51}$$

3. TURBULENCE MODELLING

The turbulence model used here is the one equation model of Baldwin and Barth [2] which is derived from the classical $k-\epsilon$ model. In the following, we give an introduction to the present implementation of the model. Further details can be found in [2].

The model solves a partial differential equation for the turbulent Reynolds number $R_t = k^2/(\nu\epsilon)$,

$$\frac{DR_t}{Dt} = (c_{\epsilon 2} f_2 - c_{\epsilon 1})\sqrt{R_t P} + \nu\left(1 + 2\frac{\nu_t}{\sigma_e}\right)\frac{\partial^2 R_t}{\partial x_i \partial x_i} - \frac{\nu}{\sigma_e}\frac{\partial}{\partial x_i}\left(\nu_t \frac{\partial R_t}{\partial x_i}\right), \tag{52}$$

where the eddy viscosity is defined as $\nu_t = c_\mu \nu R_t D_1 D_2$.

The functions D_1 and D_2 are damping functions given as

$$D_1 = 1 - \exp(-y^+/A_1^+), \tag{53}$$

$$D_2 = 1 - \exp(-y^+/A_2^+). \tag{54}$$

As assumed, ν_t or R_t is independent of z. As a consequence the derivatives in the R_t equation are taken only with respect to x and y.

The production term P is given as

$$P = \nu_t\left(\frac{\partial u_i}{\partial x_j} + \frac{\partial u_j}{\partial x_i}\right)\frac{\partial u_i}{\partial x_j}, \tag{55}$$

where the derivatives with respect to the z-direction are calculated using the hypotheses given in Subsection 2.1.

The function f_2 is defined as

$$f_2(Y^+) = \frac{c_{\epsilon 1}}{c_{\epsilon 2}} + \left(1 - \frac{c_{\epsilon 1}}{c_{\epsilon 2}}\right)\left(\frac{1}{kY^+} + D_1 D_2\right) \times \left[\sqrt{D_1 D_2} + \frac{Y^+}{\sqrt{D_1 D_2}}\left(\frac{D_2}{A_1^+}\exp\left(-\frac{Y^+}{A_1^+}\right) + \frac{D_1}{A_2^+}\exp\left(-\frac{Y^+}{A_2^+}\right)\right)\right]. \tag{56}$$

The constants used are

$$k = 0.41, \quad c_{\epsilon 1} = 1.2, \quad c_{\epsilon 2} = 2,$$
$$c_\mu = 0.09, \quad A_1^+ = 26, \quad A_2^+ = 20.$$

The boundary condition for R_t at the wall is taken equal to zero and at the inflow boundary it is put equal to 0.5.

4. NUMERICAL IMPLEMENTATION

In this section, we present the discretization of the resulting system of equations in curvilinear coordinates.

4.1. *Temporal Discretization*

A semi-implicit, combined Adams–Bashforth/Crank–Nicolson scheme is used to advance the solution in time. It consists of writing the vorticity transport equations, Eqs. (46)–(48), at time level $(n+1/2)\delta t$ and evaluating the convective-deformative and diffusion terms semi-implicitly. The terms with (F_1^c, F_2^c, F_3) and $\mathbf{u}$ are calculated explicitly at this time level by using an Adams–Bashforth extrapolation scheme. The ν_t-term appearing in the transport equations is taken at time level $n\delta t$.

Then, at each time step, a set of Helmholtz equations is obtained, with vorticity boundary conditions, as

$$\frac{2}{\delta t}\omega_x^{c*,n+1} + S_1^{n+1} = \frac{2}{\delta t}\omega_x^{c*,n} - S_1^n + 3\left(\frac{\partial F_3^n}{\partial \eta} - \frac{\alpha F_2^{c,n}}{z}\right) - \left(\frac{\partial F_3^{n-1}}{\partial \eta} - \frac{\alpha F_2^{c,n-1}}{z}\right), \quad (57)$$

$$\frac{2}{\delta t}\omega_y^{c*,n+1} + S_2^{n+1} = \frac{2}{\delta t}\omega_y^{c*,n} - S_2^n + 3\left(\frac{F_1^{c,n}}{\alpha z} - \frac{\partial F_3^n}{\partial \xi}\right) - \left(\frac{F_1^{c,n-1}}{\alpha z} - \frac{\partial F_3^{n-1}}{\partial \xi}\right), \quad (58)$$

$$\frac{2}{\delta t}\left(J^{-1}\omega_z^{*,n+1}\right) + S_3^{n+1} = \frac{2}{\delta t}\left(J^{-1}\omega_z^{*,n}\right) - S_3^n + 3\left[\frac{\alpha F_2^{c,n}}{\partial \xi} - \frac{\partial}{\partial \eta}\left(\frac{F_1^{c,n}}{\alpha}\right)\right] - \left[\frac{\alpha F_2^{c,n-1}}{\partial \xi} - \frac{\partial}{\partial \eta}\left(\frac{F_1^{c,n-1}}{\alpha}\right)\right], \quad (59)$$

$$\omega_x^c\big|_{\xi=0} = \left(\frac{\partial w}{\partial \eta} - \frac{\alpha v^c}{z} - 2x_\eta \Omega_y\right)\Big|_{\xi=0}, \quad (60)$$

$$\omega_y^c\big|_{\xi=0} = \left(\frac{u^c}{\alpha z} - \frac{\partial w}{\partial \xi} + 2x_\xi \Omega_y\right)\Big|_{\xi=0}, \quad (61)$$

$$\omega_z|_{\xi=0} = \left[\left(\frac{\partial(\alpha v^c)}{\partial \xi} - \frac{\partial}{\partial \eta}\left(\frac{u^c}{\alpha}\right)\right) \Big/ J^{-1}\right]\Big|_{\xi=0}, \quad (62)$$

where

$$S_1^{n+1} = \frac{\partial}{\partial \eta}\left(\frac{v^{c,n+1/2}\omega_x^{c*,n+1} - u^{c,n+1/2}\omega_y^{c*,n+1}}{J^{-1}}\right) - \frac{\left(u^{c,n+1/2}\omega_z^{*,n+1} - w^{n+1/2}\omega_x^{c*,n+1}\right)}{z} + \frac{\partial}{\partial \eta}\left[\frac{1}{J^{-1}}\frac{\partial}{\partial \xi}\left(\alpha \nu^{*,n}\omega_y^{c*,n+1}\right) - \frac{1}{J^{-1}}\frac{\partial}{\partial \eta}\left(\frac{\nu^{*,n}\omega_x^{c*,n+1}}{\alpha}\right)\right] + \frac{\alpha}{z}\frac{\partial\left(\nu^{*,n}\omega_z^{*,n+1}\right)}{\partial \xi}, \quad (63)$$

$$S_1^n = \frac{\partial}{\partial \eta}\left(\frac{v^{c,n+1/2}\omega_x^{c*,n} - u^{c,n+1/2}\omega_y^{c*,n}}{J^{-1}}\right) - \frac{\left(u^{c,n+1/2}\omega_z^{*,n} - w^{n+1/2}\omega_x^{c*,n}\right)}{z} + \frac{\partial}{\partial \eta}\left[\frac{1}{J^{-1}}\frac{\partial}{\partial \xi}\left(\alpha \nu^{*,n}\omega_y^{c*,n}\right) - \frac{1}{J^{-1}}\frac{\partial}{\partial \eta}\left(\frac{\nu^{*,n}\omega_x^{c*,n}}{\alpha}\right)\right] + \frac{\alpha}{z}\frac{\partial\left(\nu^{*,n}\omega_z^{c*,n}\right)}{\partial \xi}, \quad (64)$$

$$S_2^{n+1} = \frac{\left(w^{n+1/2}\omega_y^{c*,n+1} - v^{c,n+1/2}\omega_z^{*,n+1}\right)}{z} - \frac{\partial}{\partial \xi}\left(\frac{v^{c,n+1/2}\omega_x^{c*,n+1} - u^{c,n+1/2}\omega_y^{c*,n+1}}{J^{-1}}\right) + \frac{1}{\alpha z}\frac{\partial\left(\nu^{*,n}\omega_z^{*,n+1}\right)}{\partial \eta} - \frac{\partial}{\partial \xi}\left[\frac{1}{J^{-1}}\frac{\partial}{\partial \xi}\left(\nu^{*,n}\alpha\omega_y^{c*,n+1}\right) - \frac{1}{J^{-1}}\frac{\partial}{\partial \eta}\left(\frac{\nu^{*,n}\omega_x^{c*,n+1}}{\alpha}\right)\right], \quad (65)$$

$$S_2^n = \frac{\left(w^{n+1/2}\omega_y^{c*,n} - v^{c,n+1/2}\omega_z^{*,n}\right)}{z} - \frac{\partial}{\partial\xi}\left(\frac{v^{c,n+1/2}\omega_x^{c*,n} - u^{c,n+1/2}\omega_y^{c*,n}}{J^{-1}}\right)$$
$$+ \frac{1}{\alpha z}\frac{\partial\left(\nu^{*,n}\omega_z^{*,n}\right)}{\partial\eta} - \frac{\partial}{\partial\xi}\left[\frac{1}{J^{-1}}\frac{\partial}{\partial\xi}\left(\nu^{*,n}\alpha\omega_y^{c*,n}\right) - \frac{1}{J^{-1}}\frac{\partial}{\partial\eta}\left(\frac{\nu^{*,n}\omega_x^{c*,n}}{\alpha}\right)\right], \quad (66)$$

$$S_3^{n+1} = \frac{\partial}{\partial\xi}\left(u^{c,n+1/2}\omega_z^{*,n+1} - w^{n+1/2}\omega_x^{c*,n+1}\right) + \frac{\partial}{\partial\eta}\left(v^{c,n+1/2}\omega_z^{*,n+1} - w^{n+1/2}\omega_y^{c*,n+1}\right)$$
$$- \frac{\partial}{\partial\xi}\left[\alpha\frac{\partial\left(\nu^{*,n}\omega_z^{*,n+1}\right)}{\partial\xi}\right] - \frac{\partial}{\partial\eta}\left[\frac{1}{\alpha}\frac{\partial\left(\nu^{*,n}\omega_z^{*,n+1}\right)}{\partial\eta}\right], \quad (67)$$

$$S_3^n = \frac{\partial}{\partial\xi}\left(u^{c,n+1/2}\omega_z^{*,n} - w^{n+1/2}\omega_x^{c*,n}\right) + \frac{\partial}{\partial\eta}\left(v^{c,n+1/2}\omega_z^{*,n} - w^{n+1/2}\omega_y^{c*,n}\right)$$
$$- \frac{\partial}{\partial\xi}\left[\alpha\frac{\partial\left(\nu^{*,n}\omega_z^{*,n}\right)}{\partial\xi}\right] - \frac{\partial}{\partial\eta}\left[\frac{1}{\alpha}\frac{\partial\left(\nu^{*,n}\omega_z^{*,n}\right)}{\partial\eta}\right], \quad (68)$$

and

$$u^{c,n+1/2} = 1.5u^{c,n} - 0.5u^{c,n-1}, \quad (69)$$
$$v^{c,n+1/2} = 1.5v^{c,n} - 0.5v^{c,n-1}, \quad (70)$$
$$w^{n+1/2} = 1.5w^{n} - 0.5w^{n-1}. \quad (71)$$

In the above system of equations, the three vorticity components, $\omega_x^{c*,n+1}$, $\omega_y^{c*,n+1}$, and $\omega_z^{*,n+1}$ are coupled and solved simultaneously.

4.2. *Spatial Discretizations*

The equations are discretized in the transformed plane $[0, R_\xi] \times [0, 2]$ which is divided into a $N_\xi \times N_\eta$ regular mesh with spatial discretization

$$\delta\xi = \frac{R_\xi}{N_\xi}, \qquad \delta\eta = \frac{2}{N_\eta}.$$

To ensure that the discrete functions verify the conditions ($\nabla\cdot\boldsymbol{\omega} = 0$, $\nabla\cdot\mathbf{u} = 0$, $\boldsymbol{\omega} = \nabla\times\mathbf{u}$), a staggered grid is used. The first and second derivatives are discretized by a standard second-order centered difference scheme except the convective-deformative terms that are discretized by an upwind second-order QUICK scheme. The collocation points for the different unknowns are defined as shown below:

- The velocity component u^c is calculated at nodes $((i+1/2)\delta\xi,\ j\delta\eta)$ for $1 \le i \le N_\xi$, $1 \le j \le N_\eta$.
- The velocity component v^c is calculated at nodes $(i\delta\xi,\ (j+1/2)\delta\eta)$ for $1 \le i \le N_\xi$, $1 \le j \le N_\eta$.
- The velocity component ω is calculated at nodes $(i\delta\xi,\ j\delta\eta)$ for $1 \le i \le N_\xi$, $1 \le j \le N_\eta$.
- The vorticity component ω_x^c is calculated at nodes $(i\delta\xi,\ (j+1/2)\delta\eta)$ for $1 \le i \le N_\xi$, $1 \le j \le N_\eta$.
- The vorticity component ω_y^c is calculated at nodes $((i+1/2)\delta\xi,\ j\delta\eta)$ for $1 \le i \le N_\xi - 1$, $1 \le j \le N_\eta$.
- The vorticity component ω_z is calculated at nodes $((i+1/2)\delta\xi,\ (j+1/2)\delta\eta)$ for $1 \le i \le N_\xi - 1$, $1 \le j \le N_\eta$.

- The stream function ψ is calculated at nodes $(i\delta\xi,\ j\delta\eta)$ for $1 \le i \le N_\xi, 1 \le j \le N_\eta$.
- The divergence $\nabla \cdot \mathbf{u}$ is calculated at nodes $(i\delta\xi,\ j\delta\eta)$ for $2 \le i \le N_\xi, 1 \le j \le N_\eta$.
- The divergence $\nabla \cdot \boldsymbol{\omega}$ is calculated at nodes $((i+1/2)\delta\xi, (j+1/2)\delta\eta)$ for $1 \le i \le N_\xi - 1, 1 \le j \le N_\eta$.

4.3. *Resolution of the Helmholtz Equations*

In order to ensure a divergence free vorticity field, the three Helmholtz equations are solved simultaneously by a Gauss–Seidel or a Successive Line Overrelaxation (SLOR) iterative method. The latter consists of an implicit calculation in one specified direction in order to accelerate the convergence of the iterative method.

Since the convective-deformative terms are discretized semi-implicitly, three matrices, each containing 5 diagonals, have to be solved in each iteration of the SLOR method. At the points where the velocity and vorticity components are not defined, a linear or bilinear interpolation is used. Further details can be found in [15].

4.4. *Resolution of the ψ- and w-Equations*

The ψ- and w-equations are both Poisson equations. For simplicity, we consider only the ψ-equation. In general, a 2D Poisson equation can be solved easily by an ADI (*a*lternating *d*irection *i*mplicit) method or an iterative method, such as GMRES or Gauss–Seidel. Since a very strong stretching has been used in ξ-direction, this kind of method demands a lot of iterations and loses the numerical precision.

Since the grid used is periodic in the η-direction, a Fourier transformation in this direction has been applied adaptively. In Fourier space, the transformed equation takes the form

$$\frac{\partial}{\partial\xi}\left(\alpha\frac{\partial\hat{\psi}_k}{\partial\xi}\right) - \frac{\pi^2k^2}{\alpha}\hat{\psi}_k = \widehat{J^{-1}\omega_{zk}}, \tag{72}$$

for $-N_\eta/2 \le k \le N_\eta/2$. The standard second-order central difference scheme is used in the ξ-direction. The resulting matrix system is solved easily by a simple LU-factorisation.

The Fourier transformation of a function, f, is given by

$$\hat{f}_k = \frac{\delta\eta}{2}\sum_{j=1}^{N_\eta} f(j)\exp(-\pi(j-1)k\delta\eta), \qquad \text{for } -N_\eta/2+1 \le k \le N_\eta/2-1,$$

$$\hat{f}_k = \frac{\delta\eta}{4}\sum_{j=1}^{N_\eta} f(j)\exp(-\pi(j-1)k\delta\eta), \qquad \text{for } k = -N_\eta/2,\ N_\eta/2,$$

and the inverse Fourier transformation is

$$f(j) = \sum_{k=-N_\eta/2}^{N_\eta/2} \hat{f}_k \exp(\pi(j-1)k\delta\eta).$$

The integral equation for uniformity of the pressure is discretized by introducing a uniform tangential velocity v_τ or a circulation at the first points off the airfoil surface,

$$\oint_c \left[\frac{\sqrt{\alpha J^{-1}}v_\tau}{\delta t} + u^c\omega_z^* - w\omega_x^{c*} - \alpha\frac{\partial(v^*\omega_z^*)}{\partial\xi} + \alpha\dot{\Omega}_z(xx_\xi + yy_\xi)\right]d\eta = 0.$$

This additional tangential velocity serves to determine the stream function at the surface and results in an implicit Neumann condition for mode 0 of the stream function.

5. NUMERICAL RESULTS AND DISCUSSION

In the following, results for laminar flow past a rotating NACA 0015 airfoil and turbulent flow past a rotating NACA 63_2-415 airfoil are presented. The effect of rotation is elucidated by comparing quasi-3D computations to 2D computations and measurements, with the non-dimensional spanwise distance, $k=z/c$, as an additional 3D parameter.

5.1. *Quasi-3D Computations for Laminar Flows*

To demonstrate the influence of 3D rotating effects, the flow around a NACA 0015 airfoil at a Reynolds number 200 is calculated on a 129×101 O-grid with stretching coefficient $a'=0.5$.

In order to analyse the influence of the computational grid, a fine grid with 257×201 points was used in the case of an airfoil at incidence 15° and $k=6$. The pressure variation is shown in Fig. 2. From the figure it is seen that, except for a small difference at the pressure peak, the two curves are almost identical. Consequently, all the computations shown in this section are carried on the 129×101 grid.

First, steady flow at an angle of attack α equal to 15° is examined. In Fig. 3 where stream lines are shown at varying distances from the rotational axis, $k=z/c$, a decrease is seen in the size of the separated region for decreasing k. As shown in Appendix A this is expected as $w/u=O(k^{-1})$ for the boundary layer outside the separated region.

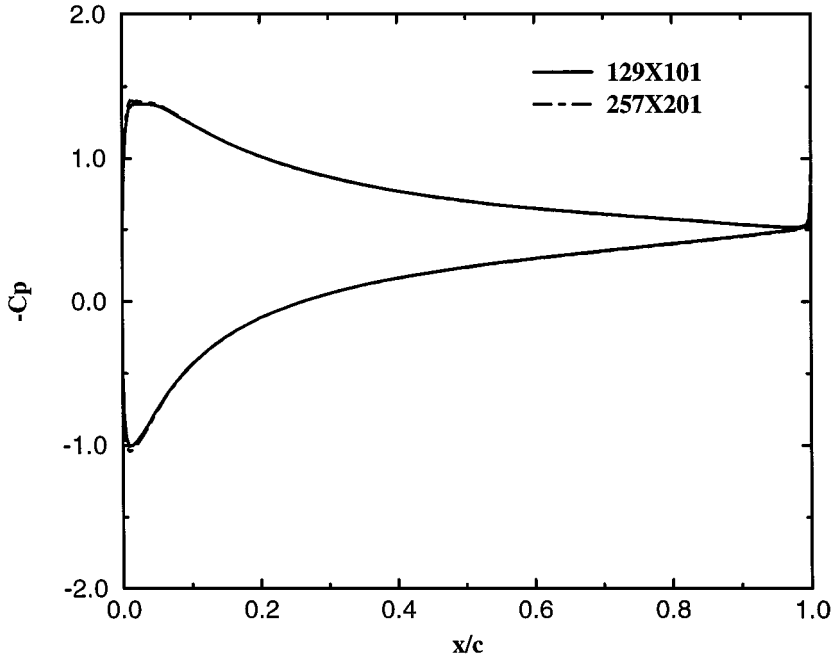

FIG. 2. The $-C_p$ variation around a NACA 0015 airfoil at incidence 15°, Re $=200$, and $k=6$.

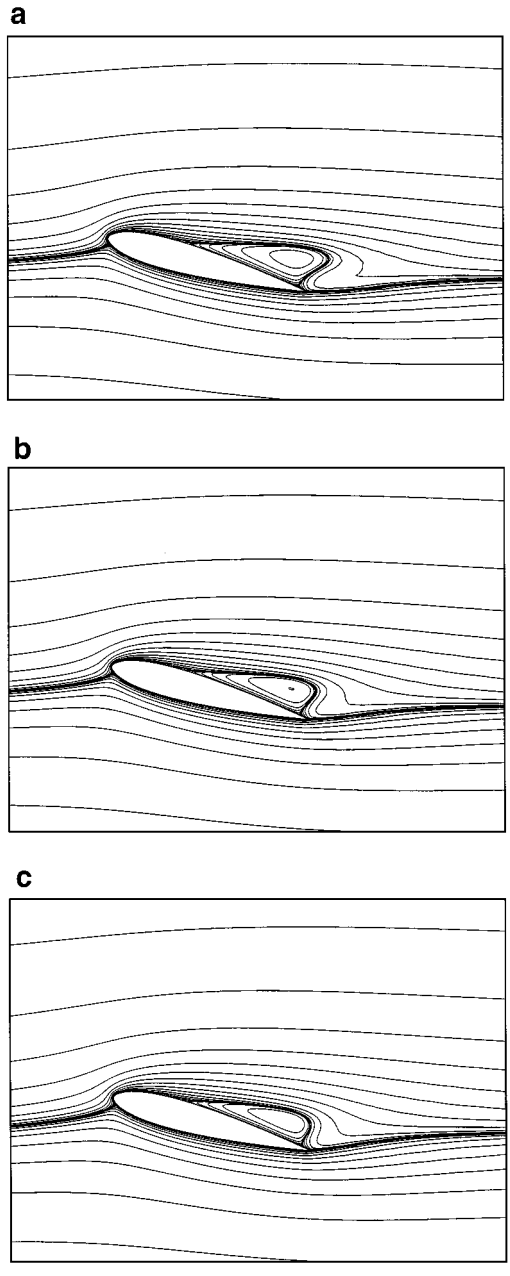

FIG. 3. Stream lines for the flow around a NACA 0015 airfoil at incidence 15° and Re = 200, (a) 2D, (b) $k = 6$, (c) $k = 4$.

Distributions of the negative pressure coefficient, $-C_p$, and skin friction coefficient, C_f, are in Fig. 4 shown at various spanwise distances, k. At the lower side of the airfoil, $-C_p$ is seen to be almost independent of k, whereas the upper side values increase when approaching the rotational axis. This corresponds to the shrinking of the separation bubble that was observed in Fig. 3 at decreasing k values. The skin friction distribution is seen to be almost identical at all spanwise distances, thus rotational effects only have an influence on the pressure distribution. Further, this influence is only significant at separation.

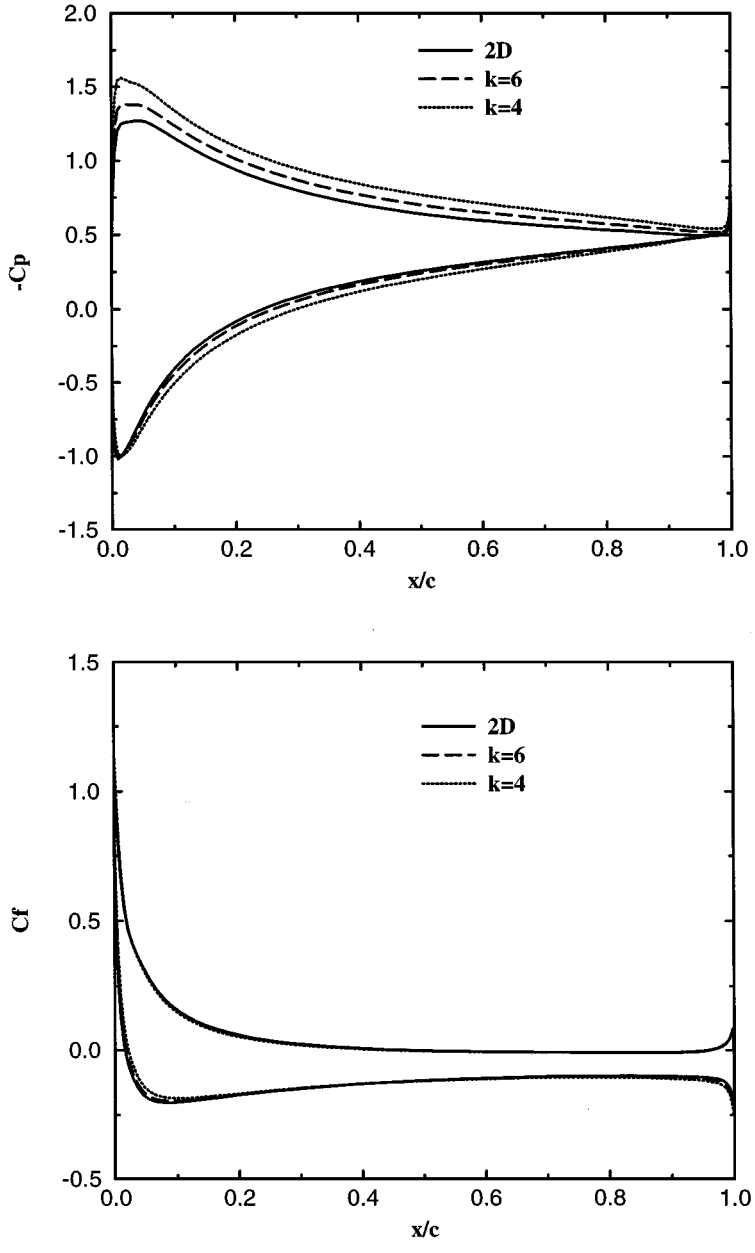

FIG. 4. The $-C_p$ and C_f distributions on a NACA 0015 airfoil at incidence 15° and Re = 200.

In Fig. 5, the streamwise vorticity component is shown for $k = 6$ and $k = 4$. From the figure, this vorticity component is seen to attain higher values at decreasing spanwise positions. The spanwise vorticity component is shown for $2D$, $k = 6$, and $k = 4$ in Fig. 6. From the figure, no big difference is seen except that the vorticity is closer to the wall at the separated region when decreasing spanwise positions (same phenomenon as in the stream line plot, Fig. 3).

Computed drag and lift coefficients C_d and C_l, respectively, at different distances k and incidences α are shown in Fig. 7. It is noted that for all incidences, decreasing the spanwise

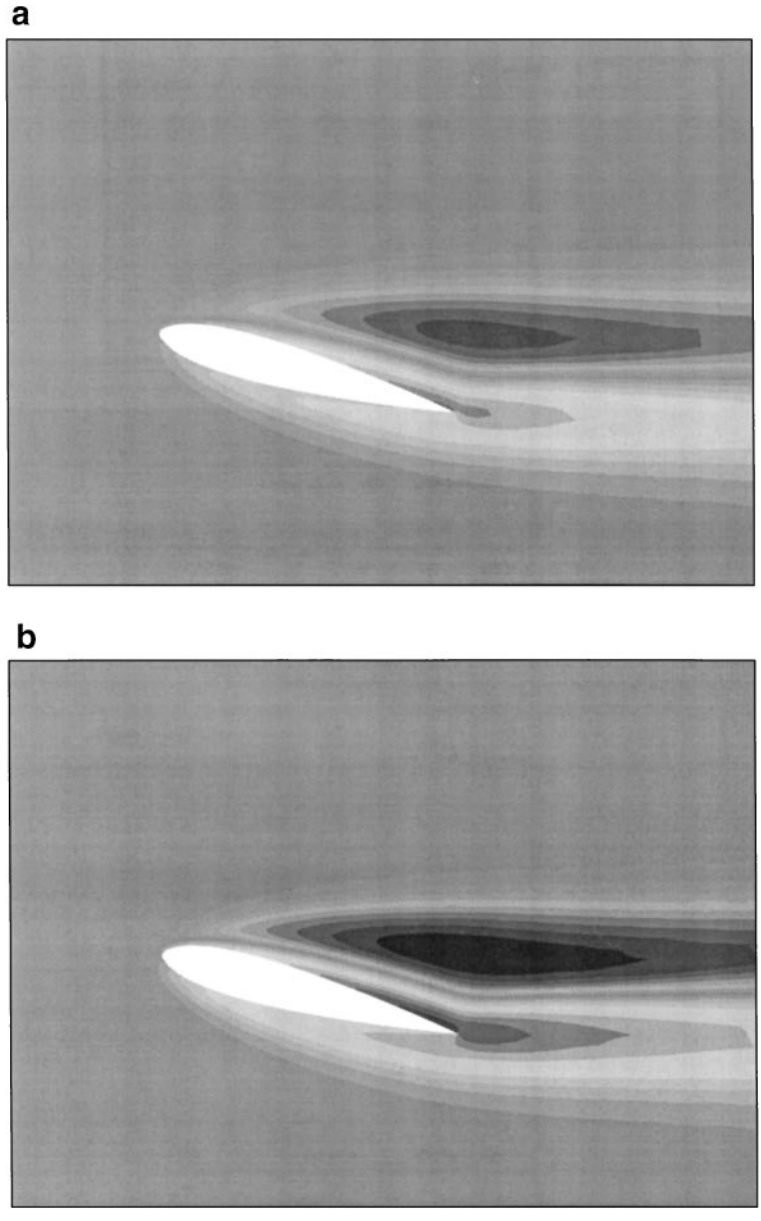

FIG. 5. Streamwise vorticity for the flow around a NACA 0015 airfoil at incidence 15° and Re = 200, (a) $k = 6$, (b) $k = 4$.

position k results in increased lift and drag coefficients. As shown by the figure, the increase in lift is more pronounced than the increase in drag. Note that in this figure, the values at incidence 25° are averaged in time because the flows have become unsteady.

5.2. *Quasi-3D Computations for Turbulent Flows*

In order to analyse the influence of 3D rotating effects on turbulent flows, the flow past a rotating NACA $63_2 - 415$ airfoil has been computed at a Reynolds number $Re = 1.5 \times 10^6$. This airfoil is widely used for wind turbine rotors, e.g., the outer part of the LM 19 wind turbine blade. The calculations are performed on a 161×101 grid using the Baldwin–Barth

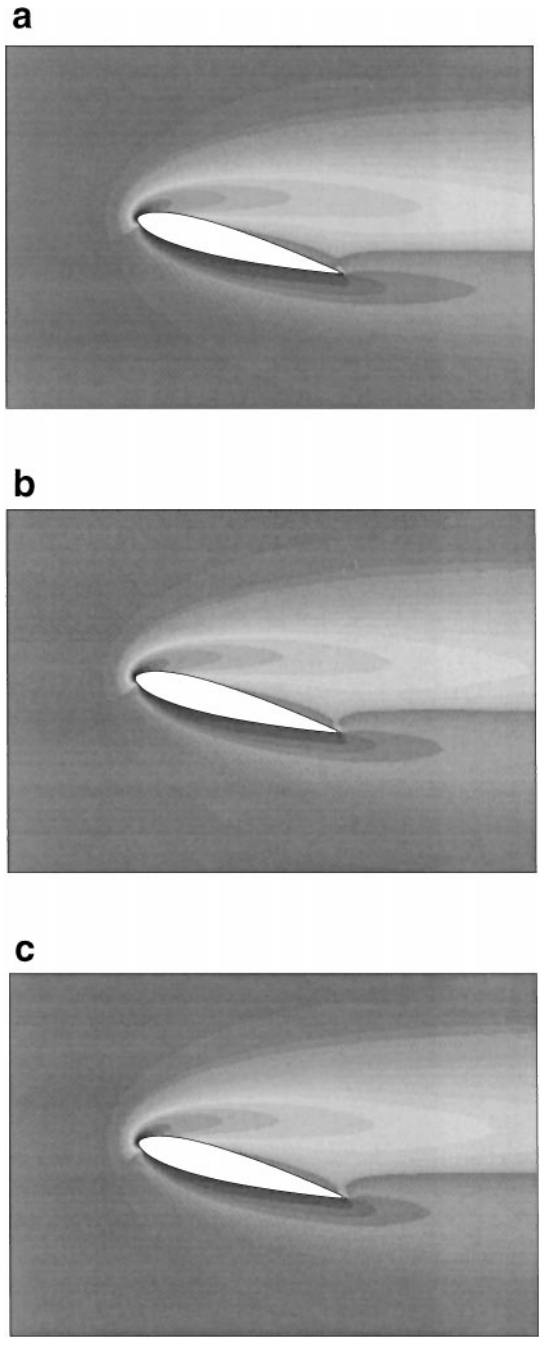

FIG. 6. Spanwise vorticity for the flow around a NACA 0015 airfoil at incidence 15° and Re = 200, (a) 2D, (b) $k = 6$, (c) $k = 4$.

turbulence model. To ensure that the first grid point off the airfoil surface is located at y^+-values less than 4, the height of the first computational cell is put equal to about $3 \cdot 10^{-5}$, resulting in a stretching coefficient $a' = 0.999$.

As a first validation of the developed code, 2D computations on a 161×101 grid were compared to experimental data [1] for incidences up to 25°. The outcome is shown in Fig. 8

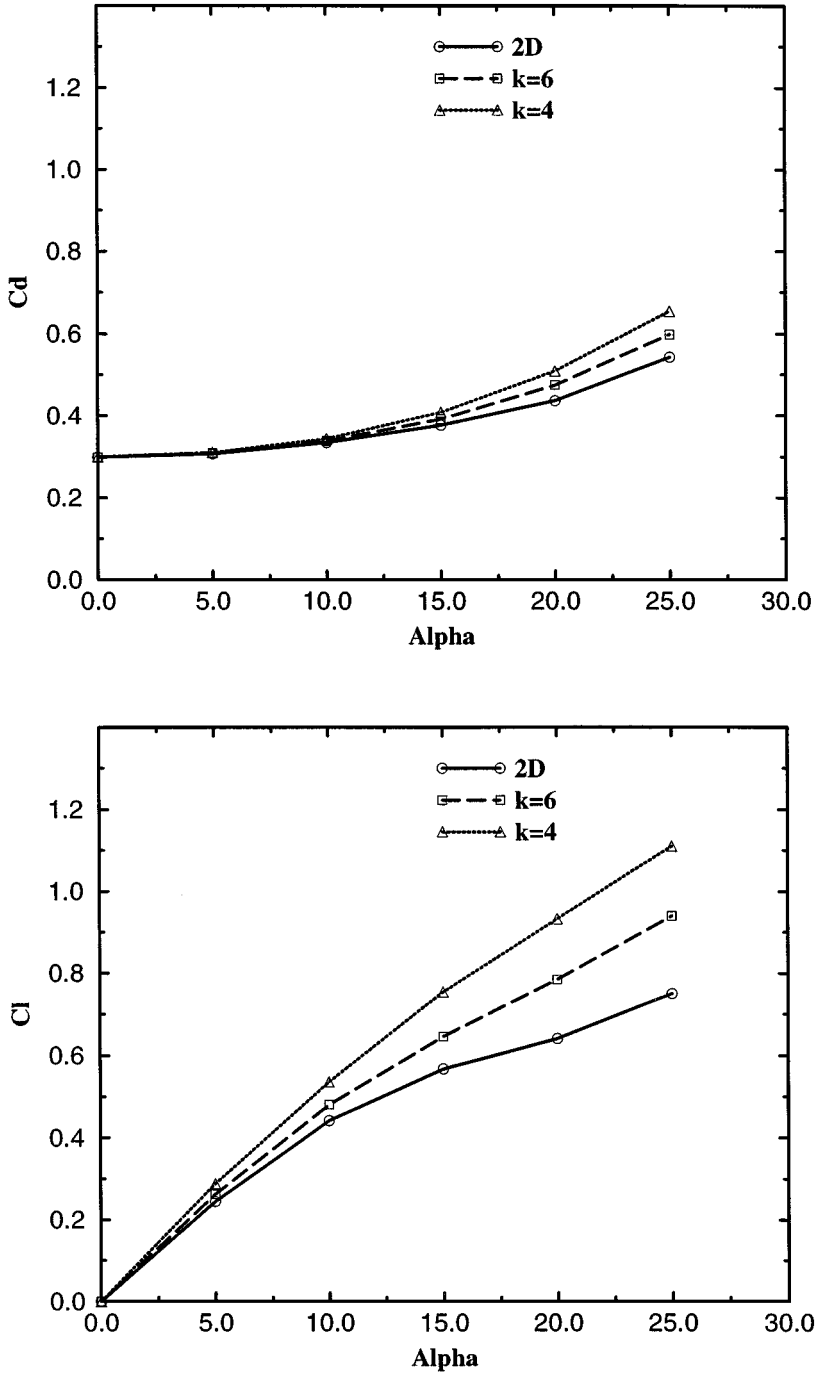

FIG. 7. C_d and C_l vs α for a NACA 0015 airfoil at $\mathrm{Re} = 200$.

where the computed C_l-distribution is compared to measured airfoil data at a Reynolds number of 3×10^6. The comparison demonstrates that the 2D version of the code in combination with the Baldwin–Barth turbulence model is capable of predicting both stall and post-stall correctly.

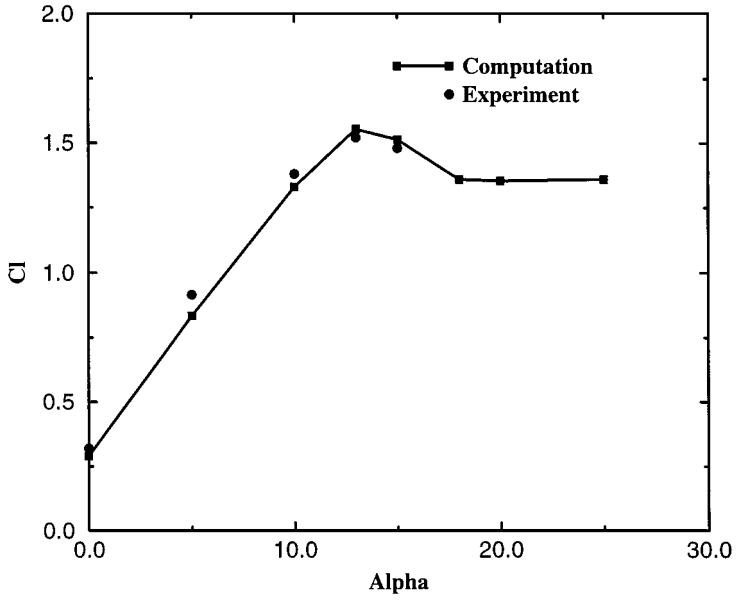

FIG. 8. Comparison of computed 2D C_l-coefficient vs α of a NACA $63_2 - 415$ airfoil at $\mathrm{Re} = 1.5 \times 10^6$ with experimental data at $\mathrm{Re} = 3 \times 10^6$.

In order to analyse the sensitivity of the grid spacing, two additional computations, one where the number of grid points was doubled in tangential direction and one with a stronger stretching of $a' = 0.9995$ in the normal direction, were carried out at an incidence of 20° and $k = 6$. The pressure variations are compared in Fig. 9. From the figure it is seen that letting the maximum distance of the first grid points away from the airfoil surface go from $y^+ = 3.5$ to $y^+ = 1.7$ does not change the pressure distribution. This is to be expected, as

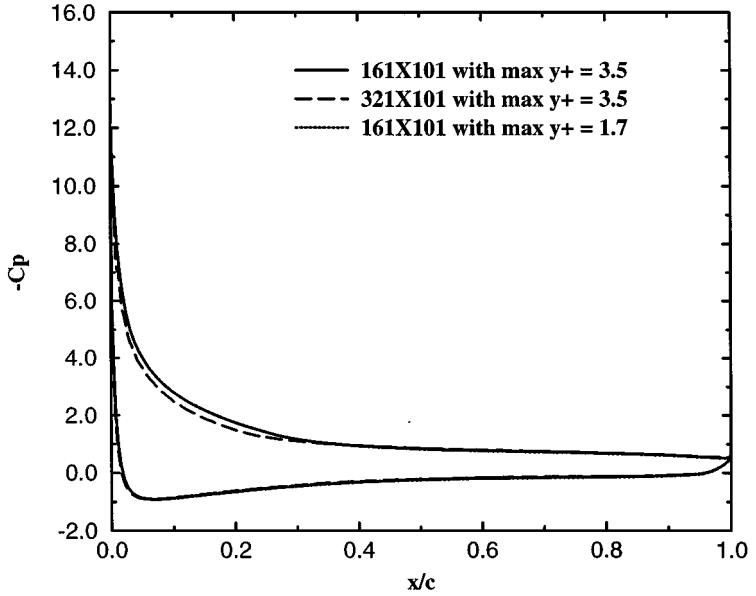

FIG. 9. The $-C_p$ variation around a NACA $63_2 - 415$ airfoil at incidence 20°, $\mathrm{Re} = 1.5 \times 10^6$, and $k = 6$.

we employ an O-grid where y^+ attains minimum values at the leading and the trailing edge. For the original mesh these values are below two. Doubling the number of the grid points in the tangential direction from 161 to 321, however, is seen to change the $-C_p$-distribution on the suction side of the airfoil. Furthermore, a weak unsteady solution appears on the fine grid. This is seen in the stream line plot in Fig. 10, where the wake line on the fine grid exhibits an unsteady undulating behaviour. The sensitivity of the grid spacing on the airfoil characteristics is summarized in Table I. From this it is seen that a further stretching in the

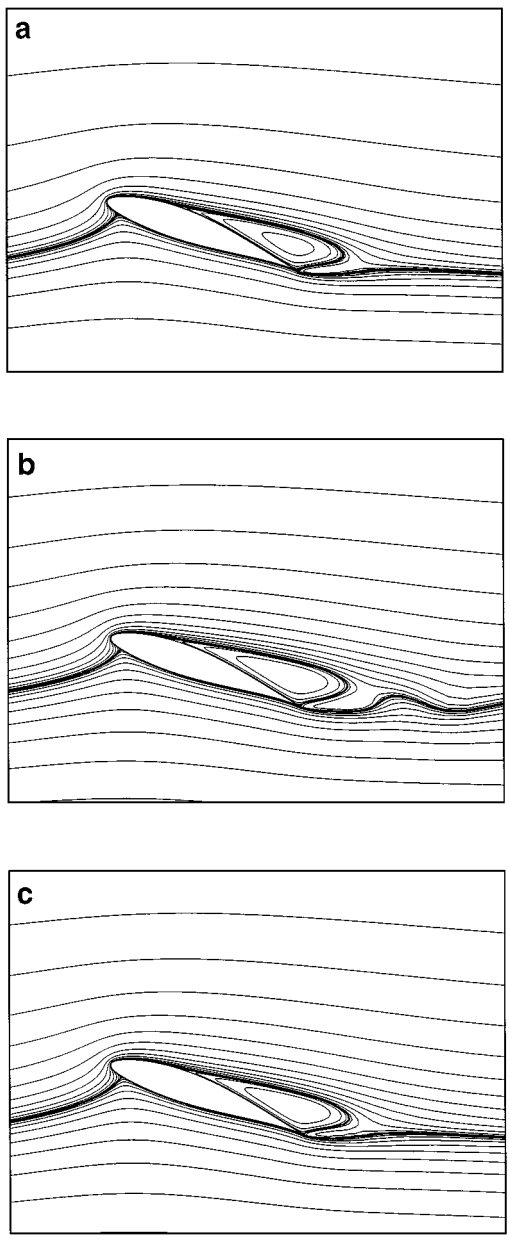

FIG. 10. Stream lines for the flow around a NACA $63_2 - 415$ airfoil at incidence 20°, $\mathrm{Re} = 1.5 \times 10^6$, and $k = 6$. (a) Results for 161×101 points with $y^+ \leq 3.5$ at the first points away from the wall; (b) 321×101 points with $y^+ \leq 3.5$ at the first points away from the wall; (c) 161×101 points with $y^+ \leq 1.7$ at the first points away from the wall.

TABLE I
Grid Refinement Study for the NACA 63_2 − 415 Airfoil at Incidence 20°, Re = 1.5×10^6 and $k = 6$

Grid	max y^+	Cd	Cl	Cm
161×101	3.5	0.13841	1.71266	−0.10335
321×101	3.5	0.15669	1.61114	−0.10991
161×101	1.7	0.13682	1.71274	−0.10252

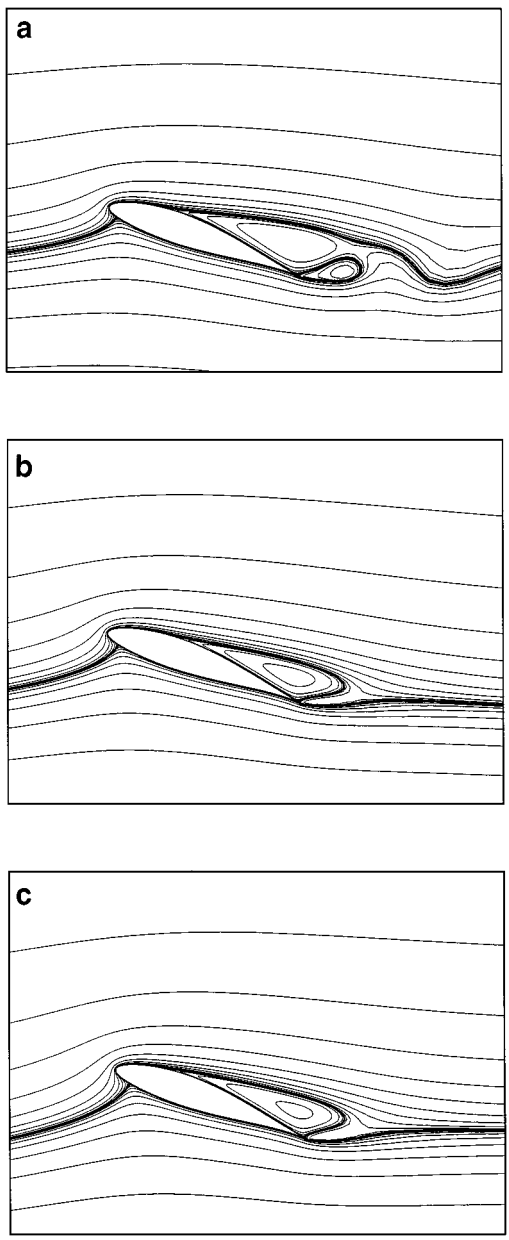

FIG. 11. Stream lines for the flow around a NACA 63_2 − 415 airfoil at incidence 20° and Re = 1.5×10^6, (a) 2D, (b) $k = 6$, (c) $k = 4$.

normal direction does not change noticeably the airfoil forces. Doubling the number of grid points in the tangential direction decreases the lift coefficient by about 6% and increases the drag coefficient by about 12%, as compared to the original mesh. Consequently, the solution is still grid-dependent, but to analyse the influence of rotational effect on the airfoil characteristics it is found to be sufficient to perform the computations on the 161×101 grid.

In order to analyse the influence of rotation on the development of separation bubbles, the flow at an incidence of 20° has been studied using the quasi-3D model. In Fig. 11, streamline plots are shown at $k = \infty(2D)$, 6, and 4. It is seen that the effect of rotation is to

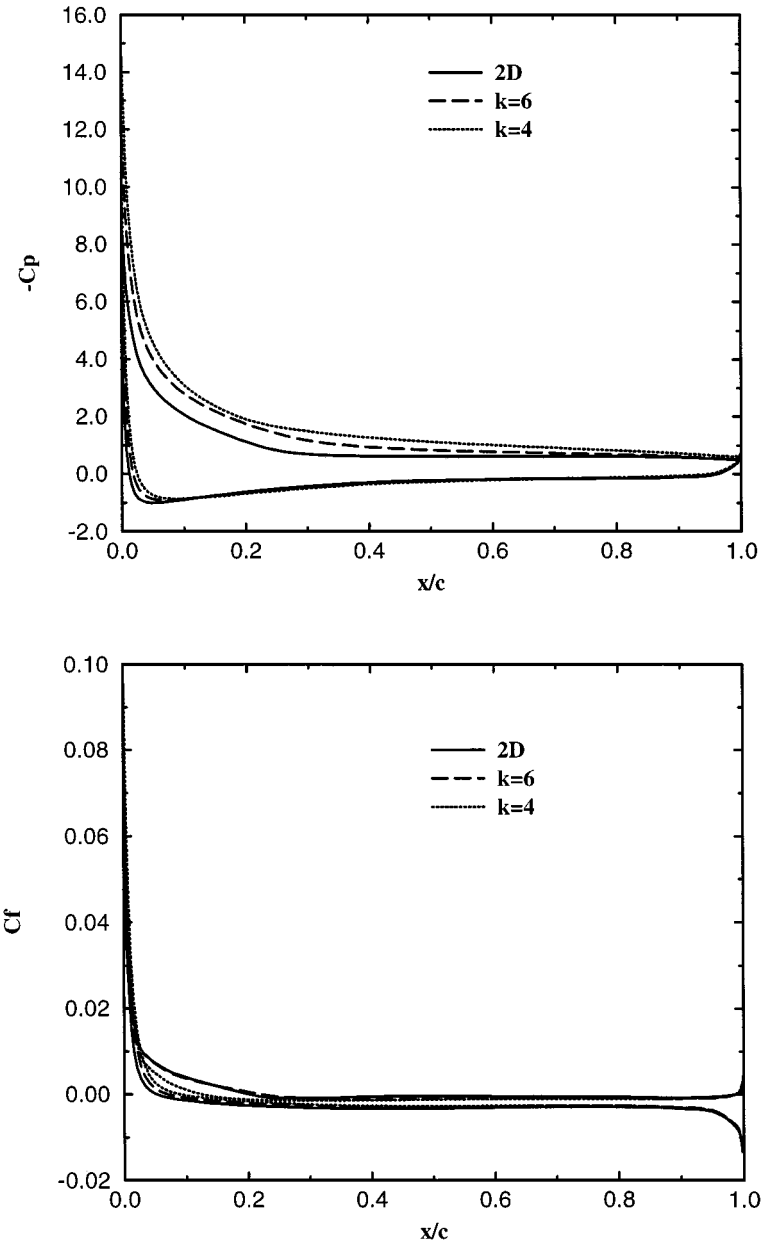

FIG. 12. The $-C_p$ and C_f distributions on a NACA $63_2 - 415$ airfoil at incidence 20° and $\mathrm{Re} = 1.5 \times 10^6$.

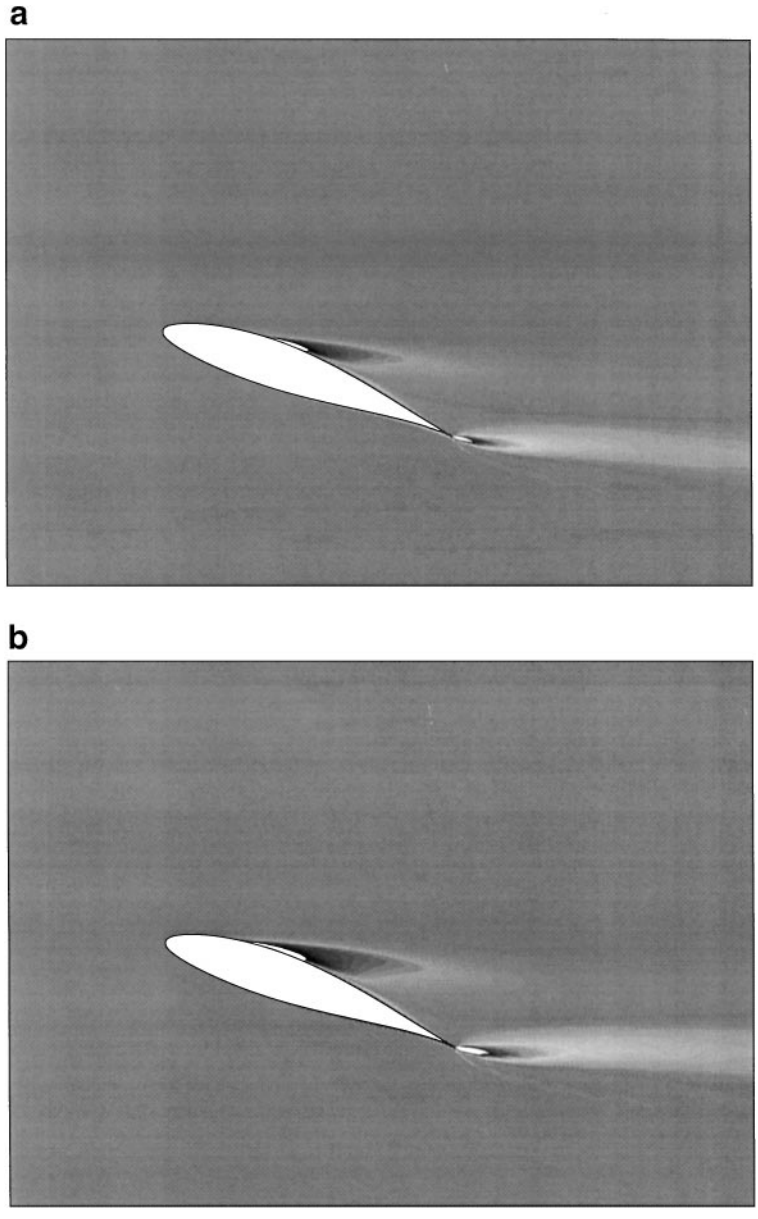

FIG. 13. Streamwise vorticity for the flow around a NACA 63_2-415 airfoil at incidence 20° and $\mathrm{Re} = 1.5\times10^6$, (a) $k = 6$, (b) $k = 4$.

stabilize vortex shedding and suppress the growth of the separation bubble. The stagnation point moves downstream and the separation moves slightly towards the leading edge when k becomes small. This phenomenon is also observed in the $-C_p$ and C_f curves in Fig. 12, where the influence of rotation is seen to be most pronounced on the $-C_p$-distribution, as was also found in the laminar case. In Fig. 13, the streamwise vorticity is shown for $k = 6$ and 4. From the figure this vorticity component is seen to attain higher values when approaching the rotational axis, i.e., for small k-values. In Fig. 14 we depict the normal force coefficient, C_n, and the tangential force coefficient, C_t, as a function of incidence. It is observed that decreasing k results in an increase in C_n and a decrease in C_t, with the

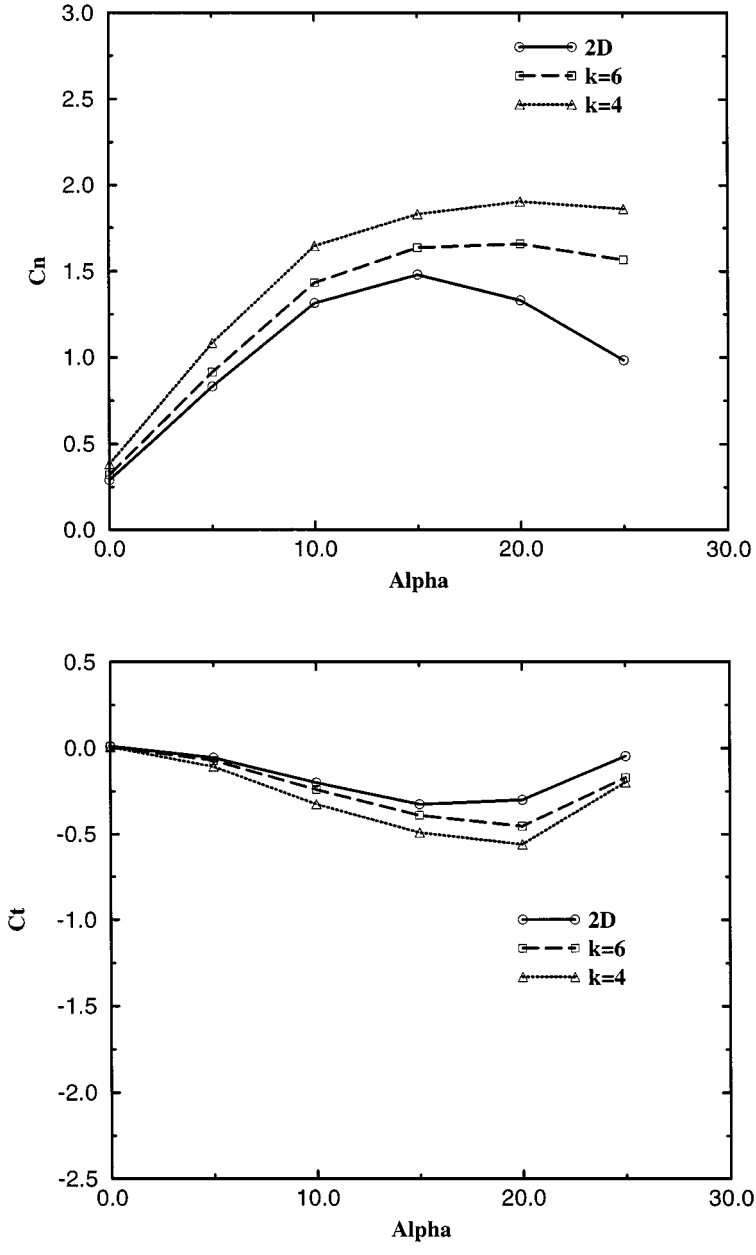

FIG. 14. C_n and C_t vs α of a NACA $63_2 - 415$ airfoil at $\mathrm{Re} = 1.5 \times 10^6$.

former being the most significant. Thus, a maximum C_n-value of about 1.4 in the 2D case is increased to approximately 1.9 at $k = 4$.

6. CONCLUSION

A quasi-3D Navier–Stokes model which takes into account rotational and 3D effects has been developed. The model enables the study of the rotational effect of a rotor blade at computing costs similar to what is typical for 2D airfoil calculations.

The model shows, both for laminar and turbulent flows, that rotational effects have an influence on the airfoil characteristics that depends on the non-dimensional spanwise distance, $k = z/c$. Thus, the effect of rotation, which becomes more pronounced as the axis of rotation is approached, is to suppress vortex shedding and the development of separation bubbles. As a consequence, decreasing the spanwise position results in an increase in both C_l and C_d.

The depicted results show that the model is capable of determining the correct qualitative behaviour for airfoils subject to rotation. It has not been possible to compare the computed results with detailed 3D experiments, as such are not available. However, the model is presently being validated against full 3D computations in order to verify the error introduced by the basic hypothesis. If it turns out that the model gives the correct behaviour, not just qualitatively as in the cases treated here, but also quantitatively, it will be a useful tool for deriving airfoil data for use in engineering predictive codes.

APPENDIX A: ORDER OF MAGNITUDE ESTIMATION OF z-DERIVATIVES

To evaluate the influence of terms containing z-derivatives we here perform an order of magnitude analysis on the flow equations in a rotating frame of reference. For simplicity we only consider the parabolized Navier–Stokes equations in chordwise and spanwise directions.

Considering a body-fitted coordinate system (s, n, z) with velocity components (u, v, w), we get continuity,

$$\frac{\partial u}{\partial s} + \frac{\partial v}{\partial n} + \frac{\partial w}{\partial z} = 0, \tag{1}$$

s-momentum,

$$u\frac{\partial u}{\partial s} + v\frac{\partial u}{\partial n} + w\frac{\partial u}{\partial z} = -\frac{1}{\rho}\frac{\partial p}{\partial s} + 2\Omega_y w\cos\theta + \Omega_y^2 s\cos^2\theta + \frac{\partial \tau_s}{\partial n}, \tag{2}$$

z-momentum,

$$u\frac{\partial w}{\partial s} + v\frac{\partial w}{\partial n} + w\frac{\partial w}{\partial z} = -\frac{1}{\rho}\frac{\partial p}{\partial z} - 2\Omega_y u\cos\theta + \Omega_y^2 z + \frac{\partial \tau_z}{\partial n}, \tag{3}$$

where θ is the angle between the tangent to the surface of the airfoil and the x-direction. The shear stresses are given as

$$\tau_s = \nu\frac{\partial u}{\partial n} - \overline{u'v'},$$

$$\tau_z = \nu\frac{\partial w}{\partial n} - \overline{v'w'},$$

with $\overline{u'v'}$ and $\overline{v'w'}$ denoting the dominant Reynolds stresses.

As the scaling laws depend on the type of flow regime considered, we here distinguish between attached and separated flows. Geometrically we scale the chordwise dimension, s, by means of the blade chord, c, and the normal dimension, n, by the boundary layer thickness, δ. The latter, however, has no influence on the analysis to be presented in the following.

A.1. *Attached Flow*

For attached flow we assume the chordwise velocity to scale with the inviscid freestream velocity,

$$u \sim \sqrt{\Omega_y^2 z^2 + U_\infty^2} = \Omega_y z \sqrt{1+\lambda^2}, \tag{4}$$

where $\lambda = U_\infty / \Omega_y z$.

From the analysis of Sears [14], we get the relation

$$w \sim \Omega_y c. \tag{5}$$

Introducing this scaling to the continuity equation we get

$$\frac{\partial w}{\partial z} \Big/ \frac{\partial u}{\partial s} \sim \left(\frac{c}{z}\right)^2 \Big/ \sqrt{1+\lambda^2}. \tag{6}$$

To estimate the order of magnitude of λ we may take $\Omega_y z = 30$ m/s, which would correspond to the mid section of a wind turbine blade that is turning with a tip speed of 60 m/s. As the wind speed ranges from 0 to about 30 m/s, we get that $\lambda \in [0, 1]$. Thus, in the continuity equation $\partial w/\partial z$ scales as $O(c/z)^2$, and can be neglected for high aspect ratio blades, where $c \ll z$.

In the momentum equations the chordwise convection terms are the leading terms for attached flow. Comparing these to the spanwise convection terms, we get

$$w\frac{\partial u}{\partial z} \Big/ u\frac{\partial u}{\partial s} \sim \left(\frac{c}{z}\right)^2 \Big/ \sqrt{1+\lambda^2}, \tag{7}$$

$$w\frac{\partial w}{\partial z} \Big/ u\frac{\partial w}{\partial s} \sim \left(\frac{c}{z}\right)^2 \Big/ \sqrt{1+\lambda^2}. \tag{8}$$

Thus, the spanwise convection terms scale as $O(c/z)^2$ and may thus be neglected for $c \ll z$.

A.2. *Separated Flow*

In separated flow regimes the chordwise pressure gradient becomes small and we here assume the Coriolis term, $2\Omega_y w \cos\theta$, to be the leading term in the s-momentum equation,

$$u\frac{\partial u}{\partial s} \sim \Omega_y w,$$

implying that

$$u \sim \sqrt{\Omega_y w c}. \tag{9}$$

In the z-momentum equation we assume the centrifugal pumping term, $\Omega_y^2 z$, to be the dominant one. The scaling then takes the form

$$O\left(u\frac{\partial w}{\partial s}\right) = O(\Omega_y^2 z),$$

implying that

$$u \sim \Omega_y^2 z c w^{-1}. \tag{10}$$

Combining (9) and (10) we get

$$u \sim \Omega_y c^{2/3} z^{1/3}, \tag{11}$$

$$w \sim \Omega_y c^{1/3} z^{2/3}, \tag{12}$$

and we may now evaluate the order of the spanwise derivatives,

$$w\frac{\partial u}{\partial z}\Big/ u\frac{\partial u}{\partial s} \sim \left(\frac{c}{z}\right)^{2/3}, \tag{13}$$

$$w\frac{\partial w}{\partial z}\Big/ u\frac{\partial w}{\partial s} \sim \left(\frac{c}{z}\right)^{2/3}, \tag{14}$$

$$\frac{\partial w}{\partial z}\Big/ \frac{\partial u}{\partial s} \sim \left(\frac{c}{z}\right)^{2/3}. \tag{15}$$

APPENDIX B: GENERATION OF ORTHOGONAL O-GRID

The orthogonal O-grid used in this paper is constructed by using a conformal mapping which is an analytical function of finite series Fourier expansion [1]. In the next sections, we present how to determine the Fourier coefficients (Appendix B.1) and the final form of conformal mapping (Appendix B.2).

B.1. *Determination of Fourier Expansion for an Airfoil Profile*

In general, any airfoil profile can be mapped to a near circle by the relation

$$z = z' + \frac{a^2}{z'}, \tag{16}$$

where $a =$ chord of airfoil/4, z is the complex variable in the airfoil plane, and z' the one in the near circle plane.

The coordinates of z and z' are defined as

$$z = x + yi, \tag{17}$$

$$z' = a\exp(\psi + i\theta). \tag{18}$$

Then, ψ and θ can be expressed in terms of x and y as

$$\cosh\psi = \frac{x}{2a\cos\theta},$$

$$\sinh\psi = \frac{y}{2a\sin\theta},$$

$$2\sin^2\theta = p + \sqrt{p^2 + \left(\frac{y}{a}\right)^2},$$

where

$$p = 1 - \left(\frac{x}{2a}\right)^2 - \left(\frac{y}{2a}\right)^2.$$

The second step is to find the relation between the near circle and a true circle. The coordinates of the true circle are defined as

$$z_0 = a\exp(\lambda + i\phi). \tag{19}$$

The transformation relating the z' plane to the z_0 plane is the general transformation

$$z' = z_0 \exp\left(\sum_1^\infty \frac{A_n + iB_n}{{z_0}^n}\right). \tag{20}$$

By definitions (18) and (19),

$$z' = z_0 \exp(\psi - \lambda + i(\theta - \phi)). \tag{21}$$

Equating the real and imaginary parts of (20) and (21), we obtain the two Fourier expansions

$$\psi - \lambda = \sum_1^\infty \left(\frac{A_n}{r^n}\cos n\phi + \frac{B_n}{r^n}\sin n\phi\right), \tag{22}$$

$$\theta - \psi = \sum_1^\infty \left(\frac{B_n}{r^n}\cos n\phi - \frac{A_n}{r^n}\sin n\phi\right), \tag{23}$$

with $r = a\exp(\lambda)$.

If ψ is specified at $2n$ equally spaced intervals in the range $0 \le \phi \le 2\pi$, the first n-orders of Fourier expansions have been taken. Then we have

$$\lambda = \frac{1}{2n}\sum_{r=0}^{2n-1}\psi_r, \tag{24}$$

where ψ_r is the value at $\phi = r\pi/n$ and

$$A_m = \frac{1}{n}\sum_{r=0}^{2n-1}\psi_r \cos\left(m\frac{r\pi}{n}\right), \tag{25}$$

$$B_m = \frac{1}{n}\sum_{r=0}^{2n-1}\psi_r \sin\left(m\frac{r\pi}{n}\right). \tag{26}$$

Ordinarily ψ is known as a function of θ, and first approximations are obtained by substitution of θ for ϕ in the relations (24)–(26). If the first approximations are not sufficiently accurate, a second approximation can be found by interpolation of ψ against ϕ. Repeating this procedure, the airfoil profile can be represented sufficiently accurate.

B.2. *Final Form of the Conformal Mapping*

In this section, the conformal mapping is generalized in the whole plane. Setting $a = 1/\exp(\lambda)$, we have the mapping from the circle $r = 1$ to the physical profile with chord $4a$. Introducing the stretching function in r-direction of the plane outside the circle

$$r = a' + (1 - a')\exp(\pi\xi),$$
$$\phi = \pi\eta,$$

where a' is a coefficient of the stretching, we have the expressions

$$\psi = \log r + \sum_{m=1}^{n} \frac{A_m}{r^m}\cos m\phi + \frac{B_m}{r^m}\sin m\phi, \tag{27}$$

$$\theta = \phi + \sum_{m=1}^{n} \frac{B_m}{r^m}\cos m\phi - \frac{A_m}{r^m}\sin m\phi, \tag{28}$$

and

$$z = z' + \frac{a^2}{z'},$$
$$z' = \exp(\psi + i\theta).$$

The metric functions of the conformal mapping $\partial x/\partial\xi$, $\partial y/\partial\xi$, $\partial x/\partial\eta$, and $\partial y/\partial\eta$ are calculated as

$$\frac{\partial x}{\partial\xi} + i\frac{\partial y}{\partial\xi} = \frac{\pi(r - a')}{r}\left(z_0 - \frac{a^2}{z_0}\right)(C_x + iC_y),$$
$$\frac{\partial x}{\partial\eta} + i\frac{\partial y}{\partial\eta} = \pi i\left(z_0 - \frac{a^2}{z_0}\right)(C_x + iC_y),$$

with

$$C_x = 1 + \sum_{m=1}^{n} \frac{-m}{r^m}(A_m\cos m\phi + B_m\sin m\phi),$$
$$C_y = \sum_{m=1}^{n} \frac{-m}{r^m}(B_m\cos m\phi - A_m\sin m\phi),$$

and inverse metric functions $\partial\xi/\partial x$, $\partial\eta/\partial x$, $\partial\xi/\partial y$, and $\partial\eta/\partial y$

$$\frac{\partial\xi}{\partial x} = \frac{r}{r - a'}\frac{C_x\,\mathrm{Re}(F) + C_y\,\mathrm{Im}(F)}{C_x^2 + C_y^2},$$

$$\frac{\partial\eta}{\partial x} = \frac{C_x\,\mathrm{Im}(F) - C_y\,\mathrm{Re}(F)}{C_x^2 + C_y^2},$$

$$\frac{\partial\xi}{\partial y} = \frac{r}{r - a'}\frac{C_y\,\mathrm{Re}(F) - C_x\,\mathrm{Im}(F)}{C_x^2 + C_y^2},$$

$$\frac{\partial\eta}{\partial y} = \frac{C_x\,\mathrm{Re}(F) + C_y\,\mathrm{Im}(F)}{C_x^2 + C_y^2},$$

with

$$F = \frac{1}{\pi(z_0 - a^2/z_0)}.$$

From these metric functions, α is independent of ϕ,

$$\alpha = \frac{r}{r - a'}.$$

ACKNOWLEDGMENTS

The present work has been supported partially by the European Commission in the framework of the Non Nuclear Energy Programme JOULE III (Contract JOR3-CT95-0007) and EFP-97, the Research Programme for Renewable Energy under the Danish Energy Agency. Some of the computer simulations were performed on the Cray C90 vector processor at the Danish Supercomputing Center, Uni-C Denmark, and were financed by the Danish Scientific Research Council.

REFERENCES

1. I. H. Abbott and A. E. Von Doenhoff, *Theory of Wing Sections* (Dover, New York, 1959).
2. B. S. Baldwin and T. J. Barth, *A One-Equation Turbulence Transport Model for High Reynolds Number Wall-Bounded Flows*, NASA TM 102847, 1990.
3. A. Bruining, G. J. W. van Bussel, G. P. Corten, and W. A. Timmer, *Pressure Distribution from a Wind Turbine Blade; Field Measurements Compared to 2-Dimensional Wind Tunnel Data*, Technical Report IW-93065R, Delft University of Technology, Institute for Wind Energy, 1993.
4. T. Cebeci, Calculation of three-dimensional boundary layers. I. Swept infinite cylinders and small cross flow, *AIAA J.* **12**(6), 779 (1974).
5. L. E. Fogarty, The laminar boundary layer on a rotating blade, *J. AeroSci.* **18**(4), 247 (1951).
6. L. E. Fogarty and W. R. Sears, Potential flow around a rotating, advancing cylindrical blade, *J. AeroSci.* **17**(9), 599 (1950).
7. H. Himmelskamp, *Profile Investigations on a Rotation Airscrew*, Technical Report, Ph.D. Dissertation, Göttingen, 1945.
8. W. J. McCroskey, *Measurements of Boundary Layer Transition, Separation and Streamline Direction on Rotating Blades*, NASA TN D-6321, April 1971.
9. D. J. Milborrow and J. N. Ross, Airfoils characteristics of rotating blades, in *IEA LS-WECS, 12th Meeting of Experts, Copenhagen, 1984*.
10. S. F. Radwan and S. G. Lekoudis, Boundary layer calculations in the inverse mode for incompressible flows over infinite swept wings, *AIAA J.* **22**(6), 737 (1984).
11. F. Rasmussen, *Blade and Rotor Loads for Vestas 15*, Report Risø, Roskilde, Denmark, 1983.
12. G. Ronsten, Static pressure measurements on a rotating and a non rotating 2.375 m wind turbine blade—Comparison with 2D calculations, in *Amsterdam EWEC, 1991* (Elsevier, Amsterdam/New York, 1991), p. 214.
13. J. M. Savino and T. W. Nyland, *Wind Turbine Flow Visualisation Studies*, Technical Report, NASA Lewis Research Center, Cleveland, OH, 1985.
14. W. R. Sears, Potential flow around a cylindrical blade, *J. Aeronaut. Sci.* **17**(3), 183 (1950).
15. W. Z. Shen and L. Ta Phuoc, Numerical method for unsteady 3D Navier–Stokes equations in velocity-vorticity form, *Comput. & Fluids* **26**(2), 193 (1997).
16. H. Snel, Scaling laws for the boundary layer flow on rotating windturbine blades, in *Proc. of the Fourth IEA Symp. on the Aerodynamics of Wind Turbines, 1991*, p. 5.1.

17. H. Snel, R. Houwink, W. J. Piers, J. Bosschers, G. J. W. van Bussel, and A. Bruining, Sectional prediction of 3D effects for stalled flow on rotating blades and comparison with measurements, in *Lübeck Travemünde EWEC, 1993* (H. S. Stephens & Assoc., March 1993), p. 395.

18. J. N. Sørensen, *Three-Level Viscous-Inviscid Interaction Technique for the Prediction of Separated Flow Past Rotating Wings*, AFM Report 86-07, Department of Fluid Mechanics, Technical University of Denmark, 1986.